Crystallization and gelation in colloidal systems with short-ranged attractive interactions

Andrea Fortini,[*] Eduardo Sanz,[†] and Marjolein Dijkstra[‡]

Debye Institute for NanoMaterials Science, Utrecht University, Princetonplein 5, 3584 CC Utrecht, The Netherlands
(Received 16 April 2008; revised manuscript received 13 June 2008; published 3 October 2008)

We systematically study the relationship between equilibrium and nonequilibrium phase diagrams of a system of short-ranged attractive colloids. Using Monte Carlo and Brownian dynamics simulations we find a window of enhanced crystallization that is limited at high interaction strength by a slowing down of the dynamics and at low interaction strength by the high nucleation barrier. We find that the crystallization is enhanced by the metastable gas-liquid binodal by means of a two-stage crystallization process. First, the formation of a dense liquid is observed and second the crystal nucleates within the dense fluid. In addition, we find at low colloid packing fractions a fluid of clusters, and at higher colloid packing fractions a percolating network due to an arrested gas-liquid phase separation that we identify with gelation. We find that this arrest is due to crystallization at low interaction energy and it is caused by a slowing down of the dynamics at high interaction strength. Likewise, we observe that the clusters which are formed at low colloid packing fractions are crystalline at low interaction energy, but glassy at high interaction energy. The clusters coalesce upon encounter.

I. INTRODUCTION

Crystallization, vitrification, and gelation in systems with short-ranged attractive interactions like colloidal particles and proteins are widely studied phenomena [1–9]. Crystallization kinetics is especially important for proteins because good crystals are necessary for the determination of their three-dimensional (3D) structure. Furthermore, crystallization of biologically active proteins can lead to diseases such as the human genetic cataract [10]. While the crystal is an equilibrium phase [11–15], gels and glasses are nonequilibrium phases that occur due to dynamical arrest [16–20]. Vitrification in a fluid of N_c hard spheres with diameter σ_c in a volume V, occurs for packing fractions $\eta = (\pi \sigma_c^3/6)N_c/V \gtrsim 0.58$ [16], while the equilibrium phase diagram predicts a stable crystal phase for $\eta > 0.545$ [21]. In the repulsive colloidal glass phase, the particles are arrested as they become localized in a "cage" formed by the surrounding spheres. Interestingly, the addition of nonadsorbing polymer, resulting in an effective attraction between the colloids, can enhance the relaxation process so that the system can crystallize. Nevertheless, for increasing attraction strengths the particles become more and more localized due to long-lived bonds between the neighboring particles until the system is arrested in an attractive glass at smaller packing fractions [19]. An arrested state at low η is often called a gel. However, the relation between gels and attractive glasses is still highly debated. In general, gels can be classified as chemical, if the particles are linked by irreversible bonds, or as physical, if the bonds are not permanent. Physical gels can form through a nonequilibrium mechanism due to the arrest of a (metastable) gas-liquid separation by the attractive glass transition [22,23]. On the other hand, equilibrium gelation can occur in systems where the gas-liquid phase separation is suppressed by, e.g., long-ranged repulsions or directional interactions [8]. For increasing contact energy these two mechanisms for the formation of physical gels continuously evolve towards a diffusion limited cluster aggregation (DLCA) that leads to chemical gels. The metastable gas-liquid separation is therefore important for the formation of nonequilibrium gels [22], and it is widely recognized as an important factor in protein crystallization [24–27]. There has been much recent experimental, theoretical, and simulation efforts to understand the equilibrium phase diagram or the kinetics and dynamics of these systems, but only a few studies explored the relationship between the equilibrium phase diagram and the underlying kinetic pathways for gelation and crystallization. Compared to previous works [28,29] we systematically determine the crystallization behavior in relation to the equilibrium phase diagram in the region of the metastable gas-liquid phase separation and we investigate the relation between crystallization and gelation.

II. MODEL AND METHOD

We study a model system of N_c hard spheres of diameter σ_c and nonadsorbing polymers with diameter σ_p described by the Asakura-Oosawa-Vrij (AOV) model [30]. The polymers induce an effective short-ranged attractive depletion interaction between the colloids [30,31]. The total interaction potential is defined as

$$\beta U_{\text{tot}}(r_{ij}) = \begin{cases} \infty, & r_{ij} < \sigma_c, \\ \beta U_{\text{dep}}(r_{ij}), & \sigma_c < r_{ij} < \sigma_c + \sigma_p, \\ 0, & r_{ij} > \sigma_c + \sigma_p \end{cases} \quad (1)$$

with

*Present address: Department of Physics, Yeshiva University, 2495 Amsterdam Avenue, New York, NY 10033, USA.

†Present address: SUPA School of Physics, JCMB The Kings Buildings, University of Edinburgh, Mayfield Road, Edinburgh EH9 3JZ, UK.

‡m.dijkstra1@uu.nl.

$$\beta U_{dep}(r_{ij}) = -\eta_p^r \frac{(1+q)^3}{q^3} \left[1 - \frac{3r_{ij}}{2(1+q)\sigma_c} + \frac{r_{ij}^3}{2(1+q)^3\sigma_c^3} \right],$$

(2)

where $r_{ij} = |\vec{R}_i - \vec{R}_j|$ is the distance between two colloidal particles with $\vec{R}_i$ the center-of-mass of colloid i, and $\beta = 1/k_B T$ with k_B the Boltzmann's constant and T the temperature. Thus the size ratio $q = \sigma_p/\sigma_c$ determines the range of the interaction. The polymer reservoir packing fraction $\eta_p^r = (\pi\sigma_p^3/6)\rho_p^r$, is proportional to the polymer density ρ_p^r in the reservoir with which our system is in osmotic contact. This parameter controls the strength of attraction. As a measure of this interaction strength we also use the contact energy $\beta U = -\beta U_{dep}(r_{ij} = \sigma_c)$ and the experimentally accessible reduced second virial coefficient $B_2^* = 1 + 3/\sigma_c^3 \int_{\sigma_c}^{\sigma_c+\sigma_p} r^2 \{1 - \exp[-\beta U_{dep}(r)]\} dr$, which is normalized by the second virial coefficient of hard spheres with a diameter σ_c. Although colloids often have a Coulombic repulsion [32] and the attractive potential in proteins is often patchy [33] our simple model captures the basic phenomena that play a role in the competition between equilibrium and nonequilibrium phases of systems with short-ranged attractions.

We determine the equilibrium phase diagram by calculating the dimensionless free energy density $f = \beta F/V$ as a function of the colloid packing fraction η_c and contact energy βU (polymer reservoir packing fraction η_p^r) with Monte Carlo simulations. We use thermodynamic integration to relate the free energy of the effective system to that of a reference system at the same colloid volume fraction η_c. To this end, we write the total free energy density as the sum of two contributions

$$f(N_c, V, \eta_p^r) = f_c(N_c, V) + f_{dep}(N_c, V, \eta_p^r),$$

(3)

where $f_c(N_c, V)$ is the free energy density of a system of N_c hard spheres in a volume V, for which we used the Carnahan-Starling expression [34] for the fluid phase, and the Hall expression [35] for the face-centred-cubic (fcc) solid phase. The free energy density f_{dep} is the contribution of the depletion potential (2) to the free energy density, and it is computed using the λ integration [36]. In order to map out the phase diagram we determine the total free energy density $f(\eta_c, \eta_p^r)$ for many state points (η_c, η_p^r) in simulations, and we employ common tangent constructions at fixed η_p^r to obtain the coexisting phases [37]. To trace the gas-solid binodal we use $N_c = 512$ particles with 15×10^4 Monte Carlo moves per particle for equilibration and 15×10^4 Monte Carlo moves per particle for production. To check the accuracy of the results few simulations were repeated using 15×10^5 Monte Carlo moves per particle for equilibration and 15×10^5 Monte Carlo moves per particle for production. To trace the metastable binodal while avoiding crystallization [37–39] we use a smaller system with $N_c = 120$ particles. To get good statistics five to ten independent Monte Carlo runs are necessary for each value of the density.

To study the dynamics of the system we perform standard Brownian dynamics (BD) simulations [40] by quenching homogeneous configurations to one of the state points indicated by the points in Fig. 1. The time step δt is chosen to be δt
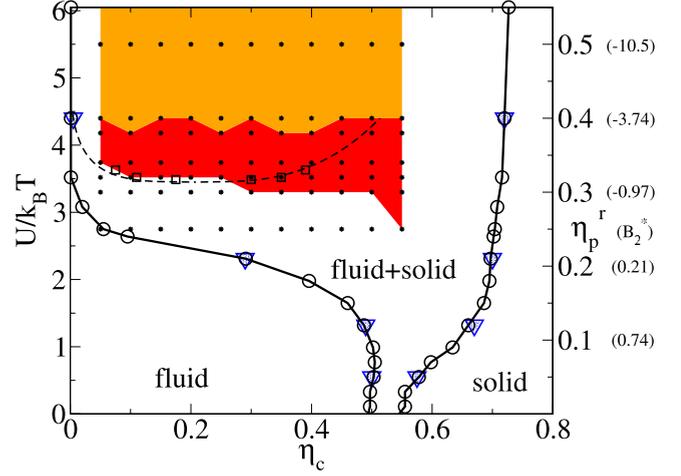

FIG. 1. (Color online) The equilibrium phase diagram of a model colloid-polymer mixture with size ratio $q = 0.15$ as a function of the colloid packing fraction η_c and interaction strength $U/k_B T$ (polymer reservoir packing fraction η_p^r and the reduced second virial coefficient B_2^*). The circles and the triangles indicate the stable fluid-solid coexistence region. (The circles are the results of simulations where a total of 3×10^4 MC moves per particles were used. The triangles are the results of more accurate simulations where a total of 3×10^5 MC moves per particles were used). The continuous lines are a guide to the eye. The squares indicate the calculated coexistence points of the gas-liquid binodal. The thin dashed line is a fit to the binodal. The points indicate the state points where we carried out BD simulations. The red (dark gray) region indicates where the crystal fraction is larger than 0.4 at $t = 600\tau_B$. The orange (light gray) region indicates where the crystal fraction is smaller than 0.4 at $t = 600\tau_B$.

$= 2 \times 10^{-5}\tau_B$ with $\tau_B = \sigma_c^2/(4D_0)$, where D_0 is the Stokes-Einstein diffusion coefficient. We neglect all hydrodynamic interactions between the particles. The random forces mimic the interaction between particles and solvent, and are sampled from a Gaussian distribution with variance $2D_0\delta t$. The random force and the dissipative term provide the system with a heat bath at constant temperature. We carry out BD simulations using particle numbers N_c ranging from 600 to 1200 and to avoid discontinuities in the potential we replace the hardcore potential with the equivalent repulsive soft potential $1/r^{36}$. We studied the evolution of a system for a total time $t = 600\tau_B$. In order to study the dynamical arrest, we compute the bond correlation function

$$\Phi_B(t) = \frac{1}{N_c} \sum_{i=1} \frac{\Sigma_{j\neq i} n_{ij}(t) n_{ij}(0)}{\Sigma_{j\neq i} n_{ij}(0)},$$

(4)

where $n_{ij} = 1$ if the separation between particle i and j is smaller than a cutoff value of $1.25\,\sigma_c$, otherwise $n_{ij} = 0$. The cutoff value corresponds to the minima between the first and second peak of the radial distribution function. The function $\Phi_B(t)$ is similar in spirit to the one used in Ref. [32], and counts which fraction of the bonds at $t = 0$ is still present at time t.

We characterize the local structure around a particle i by a set of numbers

$$q_{lm}(i) = \frac{1}{N_b(i)} \sum_{j}^{N_b(i)} Y_{lm}(\hat{r}_{ij}), \qquad (5)$$

where $Y_{lm}(\hat{r}_{ij})$ are spherical harmonics, and $\hat{r}_{ij}$ is a unit vector in the direction of the bond between particle i and particle j. The sum runs over all $N_b(i)$ neighbors of particle i. We then construct the dot product

$$q(ij) = \vec{q}_l(i) \cdot \vec{q}_l(j) = \sum_{m=-l}^{l} q_{lm}(i) q_{lm}^*(j), \qquad (6)$$

where i and j are neighboring particles and $q_{lm}^*(i)$ is the complex conjugate of $q_{lm}(i)$. We normalized the vector $\vec{q}_l(i)$, such that $\vec{q}_l(i) \cdot \vec{q}_l(i) = 1$. In our analysis particles i and j are defined as neighbors if $n_{ij} = 1$, i.e., $R_{ij} < 1.25\sigma_c$. Two particles are defined to be joined by a crystal bond if $q(ij) > 0.5$. Particle i is crystal-like if at least seven of its bonds with neighboring particles are crystal-like [41]. As in other studies [42] we use the $l=6$ order parameter.

III. RESULTS

We determine the phase diagram by calculating free energies in Monte Carlo simulations [15] for the potential (1) and for a size ratio $q=0.15$, which corresponds approximately to the experimental value of recent work [43]. Figure 1 shows the equilibrium phase diagram in the contact energy βU (polymer reservoir packing fraction η_p^r), colloid packing fraction η_c representation. For $\beta U=0$ we recover the hard-sphere phase diagram with a fluid phase at $\eta_c \simeq 0.494$ in coexistence with a face-centered-cubic (fcc) crystal phase at $\eta_c \simeq 0.545$. For increasing βU the region of fluid-solid coexistence opens up. At the critical energy $\beta U_{cr} \simeq 3.48[(\eta_p^r)_{cr} \simeq 0.316]$ we find a gas-liquid transition which is metastable with respect to a broad fluid-solid coexistence.

In order to follow the crystallization, we characterize the local structure around particle i by the q_6 order parameter [41]. We define the crystal fraction $f_{cr}(t)$ as the number of crystal-like particles at time t divided by the total number of particles. The red (dark gray) region in Fig. 1 indicates the state points for which the crystal fraction is larger than 0.4 at $t=600\tau_B$ while the orange (light gray) region indicates a fraction of crystal smaller than 0.4. Let us discuss first the low βU limit of the red (dark gray) region. Clearly, at low density the metastable gas-liquid binodal has a dramatic effect in inducing (spontaneous) crystallization of the colloidal particles, with the bottom boundary of the crystallization region as denoted by the red (dark gray) region in Fig. 1 coinciding with the metastable gas-liquid binodal. Below the binodal line, and at low colloid density, we do not observe spontaneous nucleation, in agreement with the observations of Ref. [29]. Neither do we observe, in the time scale of our simulations, crystallization just below to the critical point despite the presence of critical fluctuations that lower the nucleation barrier [44]. On the other hand, at medium-high colloid density we also observe crystallization outside the binodal. We now focus on the high βU limit for crystallization. Figure 2 shows that the crystal fraction slowly decays to zero for increasing attractive energy βU, and that the crystal fraction
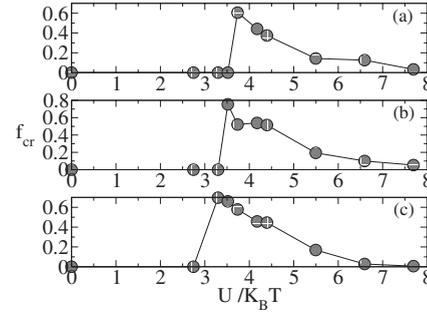

FIG. 2. Crystal fraction f_{cr} at $t=600\tau_B$ as a function of the interaction energy $U/k_B T$ for (a) $\eta_c = 0.10$. (b) $\eta_c = 0.25$. (c) $\eta_c = 0.40$.

does not depend strongly on η_c for fixed βU. This indicates a crystallization process hindered by a slowing down of the dynamics. The boundary between the orange (light gray) and red (dark gray) regions in Fig. 1 is a horizontal line at $\beta U \approx 4.4$. As has been demonstrated for short-ranged attractive systems, isodiffusivity lines are also horizontal when approaching the gas-liquid binodal [8,28]. Therefore, the slow decrease of crystallinity can be seen as an indicator of the proximity of the (attractive) glass transition line that intersects the gas-liquid binodal. It is worthwhile noting that the attractive glass transition was determined to be at $\eta_p^r \simeq 0.43$ using the long-time scaling of the incoherent correlation functions obtained from computer simulations for a system with a size ratio of $q=0.1$, and using a pair potential that included a long-range repulsive barrier to prevent gas-liquid phase separation [45]. This value is remarkable close to our value of $\eta_p^r \sim 0.4$ for which we find hardly any crystallization.

Figure 3 shows the phase diagram as in Fig. 1 but we label state points that will be discussed below. To demonstrate the existence of a dynamical arrest we compute the bond correlation function $\Phi_B(t)$ (Fig. 4) measured starting at
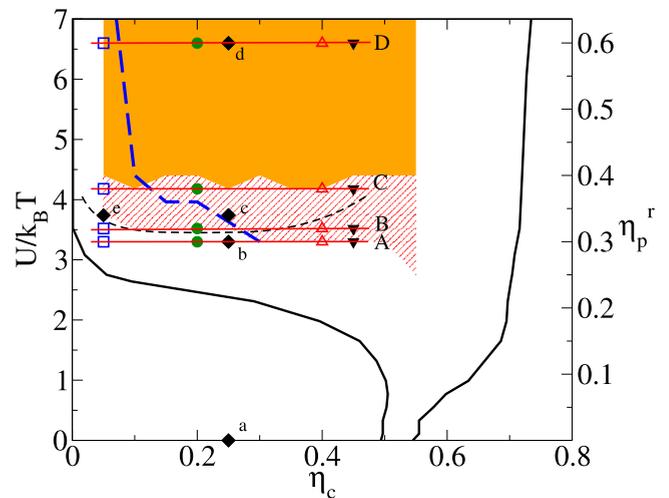

FIG. 3. (Color online) The same as Fig. 1, but we indicate the state points discussed in the text. For clarity the binodal symbols are removed. The thick (blue) dashed line indicates the transition between percolating and non-percolating states.
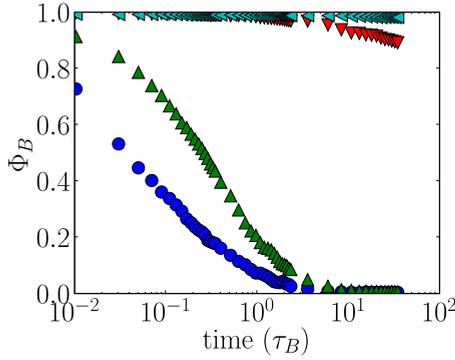
FIG. 4. (Color online) Bond correlation functions $\Phi_B(t)$ as a function of time t for $\eta_c=0.25$. Circles indicate results for energy $\beta U=0$ (point a in Fig. 3), up triangles indicate $\beta U=3.3$ (point b in Fig. 3), down triangles indicate $\beta U=3.74$ (point c in Fig. 3), triangle-left indicate $\beta U=6.6$ (point d in Fig. 3).

a time $t=600\tau_B$ after the initial quench in the state points a–d in Fig. 3. We observe a divergence in the characteristic decay time between $\beta U=3.3$ (point b in Fig. 3 and $\beta U=3.74$ (point d in Fig. 3), giving evidence of a fluid-solid (either crystal-line or amorphous) transition. The behavior of $\Phi_B(t)$ is very similar whether the solidification is due to crystallization ($\beta U=3.74$) or an attractive glass transition ($\beta U=6.6$).

We now focus our attention to the state points inside the gas-liquid region. We find that in certain regions of the phase diagram the phase separation is arrested in a permanently percolated structure. The thick dashed line in Fig. 3 corre-sponds to the percolation limit. For quenches inside the gas-liquid coexistence we find, on the left side of the percolation line, clusters that are crystalline at low βU [red (dashed) region in Fig. 3] and amorphous at high βU [orange (light gray) region in Fig. 3], while on the right-hand side, we find a "long-lived" percolating network (gel) with high-density branches that are crystalline at low βU [red (dashed) region in Fig. 3] and amorphous at high βU [orange (light gray) region in Fig. 3].

We now analyze in more detail the kinetic pathways in different regions of the phase diagram. The first state point we consider is point e in Fig. 3 ($\eta_c=0.05$, $\beta U=3.74$, and $\eta_p^r=0.34$), just beyond the gas binodal. The direct path to the equilibrium phase would be nucleation of the crystal phase in the dilute fluid phase. The actual kinetic pathway is shown in the attached movies [46]. Figures 5(a) and 5(b) show typical configurations at $t=50\tau_B$ and $t=600\tau_B$, respectively. We ob-serve first in Fig. 5(a) the formation of metastable liquid droplets (small yellow light spheres) surrounded by gas par-ticles (large light spheres). Subsequently the nucleation of the crystal (large red dark spheres) starts within the fluid droplets. The crystalline clusters grow until a local equilib-rium between the cluster and a surrounding gas phase is reached. These metastable clusters survive for a long time [Fig. 5(b)] due to low diffusion, but irreversibly coalesce upon touching, in contrast with the findings of Ref. [43]. At higher colloid density $\eta_c=0.25$ and $\beta U=3.74$ (point c in Fig. 3), we observe spinodal decomposition, and subsequently nucleation of crystal nuclei within the fluid branches of the spinodal structure. The crystalline clusters grow until the
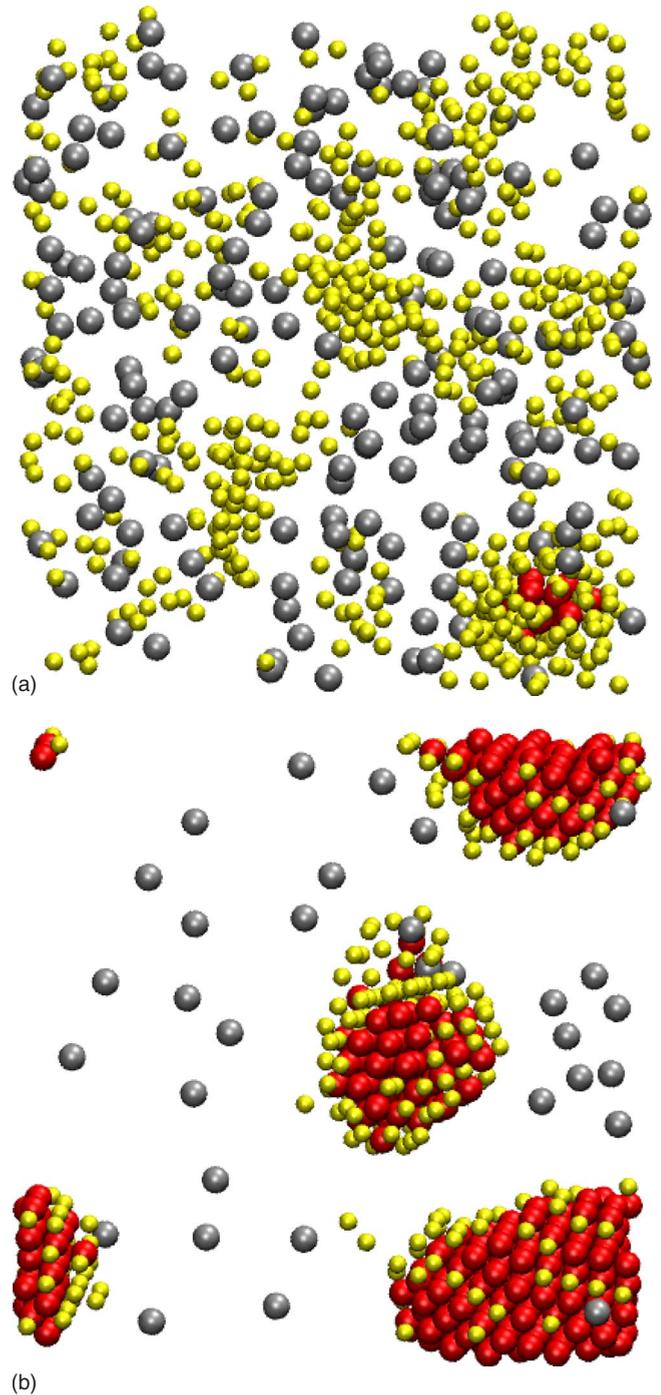

FIG. 5. (Color online) Typical snapshots for the state point e in Fig. 3 ($\eta_c=0.05$ and $\beta U=3.74$) at $t=50\tau_B$ (a) and at $t=600\tau_B$ (b). Gas particles are indicated by large light gray spheres, fluid par-ticles are indicated by yellow (small light gray) spheres and crystal particles are indicated by blue (large dark gray) spheres. The com-plete kinetic pathway is shown in the attached movies [46].

whole spinodal structure is crystalline. Figure 6(a) shows that the spinodal structure is arrested by crystallization. At higher interaction strength $\beta U=6.6$ and $\eta_c=0.25$ (point d in Fig. 3), we observe spinodal decomposition, and only very small crystal nuclei appear within the fluid branches of the spinodal structure. The spinodal decomposition is arrested
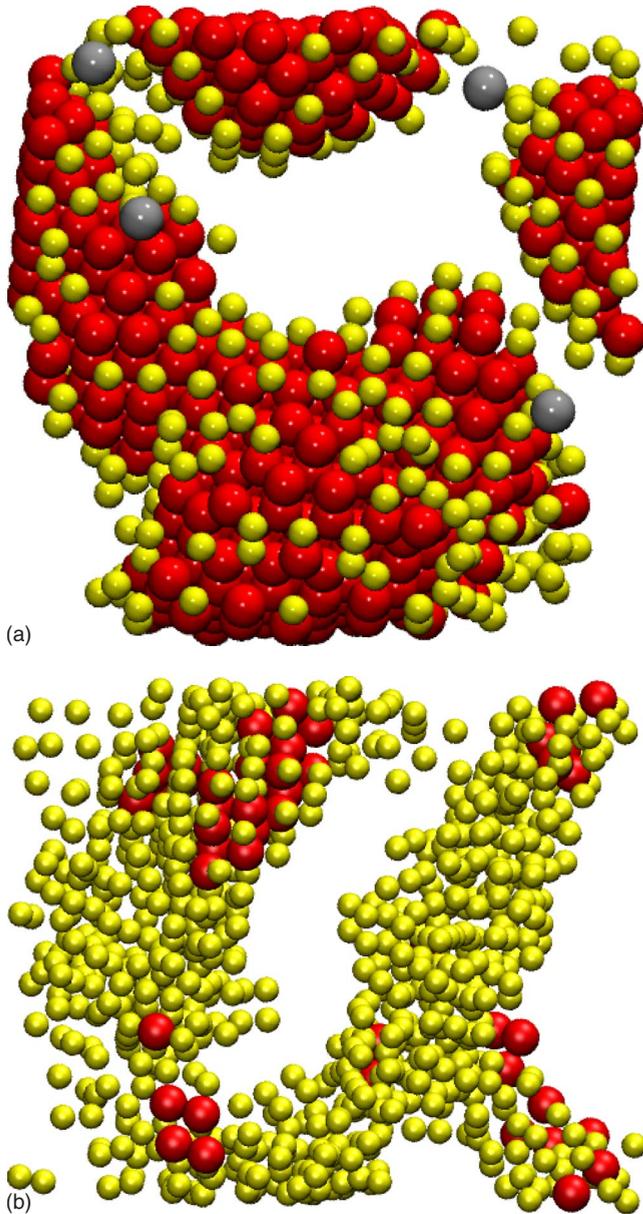
FIG. 6. (Color online) A snapshot for state point c in Fig. 3 ($\eta_c=0.25$ and $\beta U=3.74$) at $t=600\tau_B$) (a) and for state point d in Fig. 3 ($\eta_c=0.25$ and $\beta U=6.6$) at $t=600\tau_B$ (b). Gas particles are indicated by large light gray spheres, fluid particles are indicated by yellow (small light gray) spheres and crystal particles are indicated by blue (large dark gray) spheres. The complete kinetic pathway is shown in the attached movies [46].

into a branched gel by the formation of a glassy solid [Fig. 6(b)]. This scenario is consistent with nonequilibrium gelation induced by spinodal decomposition arrested by an attractive glass transition. The metastable gas-liquid phase separation is arrested due to decreased diffusion of single particles by crystallization at low βU. On the other hand, at high βU the phase separation is arrested by a slow dynamics that is consistent with vitrification, but we do not explicitly calculate the exact location of the glass transition here.

Figure 7 shows the crystal fraction $f_{cr}(t)$ as a function of time t for $\beta U=3.3$, 3.52, 4.18, and 6.6 and for varying η_c

(filled symbols along the red lines A–D in Fig. 3). The evolution of the crystal fraction is characterized by three distinct regimes. In the first regime the fraction of crystal is equal to zero. This regime corresponds to the time elapsed between the quench and the formation of a critical nucleus (induction time). The second regime corresponds to the fast growth of the crystal. Figure 7(a) shows that for state points $\eta_c=0.05$, 0.20, and 0.40 of line A in Fig. 3, the induction time is significantly different from zero. We note here that the induction time is larger than $600\tau_B$ for $\eta_c=0.05$ and 0.20. All these state points are outside the metastable gas-liquid binodal region. In Fig. 7(b), we find that state point $\eta_c=0.05$ of line B in Fig. 3 shows no crystallization at all, and hence the induction time is again larger than $600\tau_B$. This state point also lies outside the gas-liquid coexistence region, i.e, $\eta_c < \eta_c^{\rm sat}$, where $\eta_c^{\rm sat}$ denotes the coexisting packing fraction of the metastable gas phase. For quenches to $\eta_c > \eta_c^{\rm sat}$, i.e., $\eta_c=0.20$, 0.40, and 0.45, we find that the induction time is close to zero. Similarly, for quenches inside the gas-liquid spinodal as shown in Figs. 7(c) and 7(d) corresponding to line C and D in Fig. 3, the induction time is also close to zero as the formation of the spinodal structure is followed immediately by nucleation of small crystallites and subsequent growth of the crystals. In this case, the induction time is related to the spinodal decomposition $\simeq \tau_D$ [23] that is not visible on the time scale of Fig. 7. To summarize, we find that the induction time is close to zero for all quenches beyond the gas binodal of the metastable gas-liquid coexistence region, i.e., for $\eta_c > \eta_c^{\rm sat}$. The fraction of crystal grows rapidly after the induction time due to the huge difference in chemical potential between the liquid and the growing crystal phase. In the third regime, the crystal fraction grows slowly by coarsening and defect removal processes. The fraction of crystal reached by the system depends strongly on the contact energy. At low βU particle diffusion is fast enough for crystallization. On the other hand, at high βU the particles diffuse slowly and despite the thermodynamic drive to form the crystal the system is trapped in an amorphous solid. To summarize, for state points inside the binodal we always observe an induction time equal to zero, consistent with the nucleation of small crystallites in the initial stage, and subsequent growth of the crystals. Outside the binodal, the induction time is close to zero only at high colloid packing fraction. Furthermore, we observe that the fraction of crystal is independent of the packing fraction for fixed βU, while it decreases for increasing contact energy βU.

IV. CONCLUSIONS

The objective of this work was to systematically study the relationship between equilibrium and nonequilibrium phases in systems with short-ranged attractions. To study the dynamics of the system we carried out BD simulations by quenching a homogeneous fluid phase to certain state points in the phase diagram.

First, we find a window of enhanced crystallization that is delimited at high contact energy by low diffusion and at low contact energy (below line A Fig. 8) by a high nucleation barrier. Second, we observe that the crystallization is en-
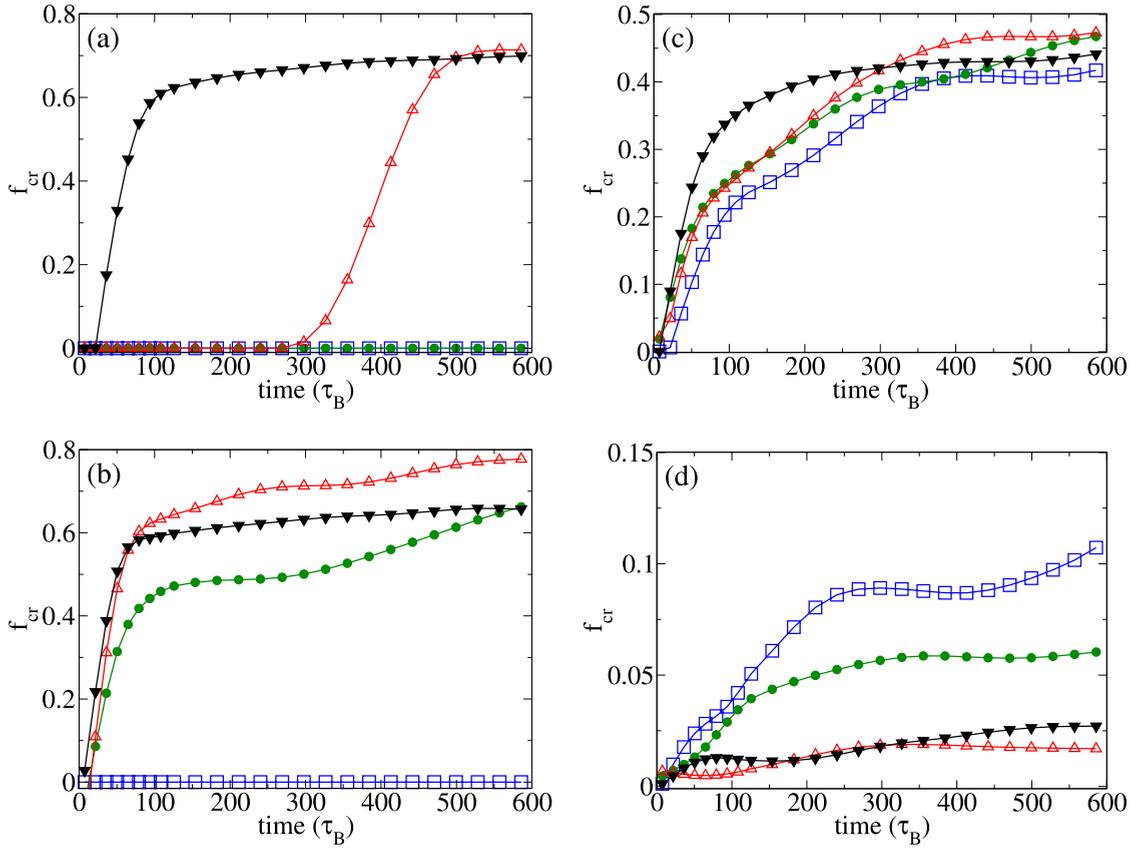
FIG. 7. (Color online) Crystal fraction f_{cr} as a function of time t for (a) $\beta U = 3.3$ (line A in Fig. 3), (b) $\beta U = 3.52$ (line in B Fig. 3), (c) $\beta U = 4.18$ (line in C in Fig. 3), (d) $\beta U = 6.6$ (line D Fig. 3). Squares indicate a colloid packing fraction $\eta_c = 0.05$, circles indicate $\eta_c = 0.20$, up triangles indicate $\eta_c = 0.40$, and down triangles indicate $\eta_c = 0.45$ (same symbols as in Fig. 3).

hanced by the metastable gas-liquid phase separation, as demonstrated by the fact that the line of spontaneous crystallization (line A in Fig. 8) at low density follows closely the
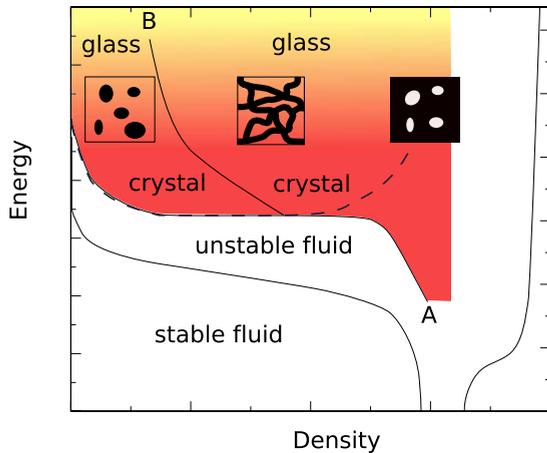

FIG. 8. (Color online) Sketch of the phase diagram in the energy-density representation reporting the location of the nonequilibrium phases found in this work. Line A is the line of spontaneous crystallization while line B indicates the transition form a cluster phase to a gel. The square insets sketch the mesoscopic morphology of the system [clusters, percolating network (gel) and porous solid from left to right]. The shading indicate the transition from a more crystalline phase (dark red) to a more amorphous one (light yellow).

binodal of the gas-liquid separation (dashed line in Fig. 8). The effect is caused by the two-step process crystallization process inside the gas-liquid binodal: the system first forms liquid domains, either through nucleation or spinodal decomposition; subsequently, crystal nucleation occurs within the dense liquid domains. This process follows the Ostwald rule of stages that states that the transition from one phase to another may proceed via intermediate metastable states. Hence, the effective nucleation rate of the crystal depends on the nucleation rate of the liquid in the gas and the crystal in the liquid phase. This two-stage crystallization process was also observed in proteins [25,26].

Last, we find two competing mechanisms of arrest of the gas-liquid spinodal decomposition. At low βU, we observe that crystallization starts within the liquid branches before the spinodal structure can coarsen into macroscopic phase separation. The crystallization slows down the coarsening process and arrests the system in structures typical of spinodal decomposition. For higher βU, the system becomes amorphous as crystallization is inhibited. This result supports a gelation caused by a glass transition that meets the liquid binodal and thereby arrests the gas-liquid phase separation [22]. We find that crystallization and vitrification are both responsible for the formation of arrested spinodal patterns (gels), albeit at different interaction energies. These two mechanisms are also responsible for the formation of two different types of long-lived but transient clusters at low colloid density. The clusters are crystalline at low βU and

glassy at high βU. At high colloid density, on the right-hand side of the gas-liquid binodal, the amorphous arrested phase is structurally very similar to a (porous) attractive glass, while the crystalline arrested phase can be seen as a polycrystalline porous material. Figure 8 shows schematically the location of the different type of phases we found in relation to the equilibrium phase diagram.

Finally, we point out that our phase diagram can provide a guide to experimentally obtain and control the morphology of crystals of colloids or proteins. The crystallization window can be located experimentally since it is delimited at low temperature by an arrested phase with liquidlike local structure and at high temperature by a mobile fluid phase. Thus, by changing the temperature it is possible to control the degree of crystallinity. The highest fraction of crystal is obtained for state points in the lower interaction strength (higher temperature) part of the crystallization window. For increasing interaction strength (decreasing temperature) the crystal fraction decreases. For the range of packing fractions studied in this work ($\eta_c < 0.55$), the colloid packing fraction does not influence the fraction of crystal or the growth rate, but has a strong influence on the morphology of the final phase. While at very low η_c clusters form, a branched structure is obtained at intermediate packing fractions, and porous materials are obtained at high η_c.

[1] M. T. A. Bos and J. H. J. van Opheusden, Phys. Rev. E **53**, 5044 (1996).

[2] N. A. M. Verhaegh, D. Asnaghi, and H. Lekkerkerker, Physica A **264**, 64 (1999).

[3] E. H. A. de Hoog, W. K. Kegel, A. van Blaaderen, and H. N. W. Lekkerkerker, Phys. Rev. E **64**, 021407 (2001).

[4] V. J. Anderson, E. H. A. de Hoog, and H. N. W. Lekkerkerker, Phys. Rev. E **65**, 011403 (2001).

[5] J. Bergenholtz, W. C. K. Poon, and M. Fuchs, Langmuir **19**, 4493 (2003).

[6] H. Sedgwick, K. Kroy, A. Salonen, M. Robertson, S. Egelhaaf, and W. Poon, Eur. Phys. J. E **16**, 77 (2005).

[7] S. Manley, H. M. Wyss, K. Miyazaki, J. C. Conrad, V. Trappe, L. J. Kaufman, D. R. Reichman, and D. A. Weitz, Phys. Rev. Lett. **95**, 238302 (2005).

[8] E. Zaccarelli, J. Phys.: Condens. Matter **19**, 323101 (2007).

[9] A. E. Bailey *et al.*, Phys. Rev. Lett. **99**, 205701 (2007).

[10] A. Pande, J. Pande, N. Asherie, A. Lomakin, O. Ogun, J. King, and G. B. Benedek, Proc. Natl. Acad. Sci. U.S.A. **98**, 6116 (2001).

[11] A. P. Gast, C. K. Hall, and W. B. Russel, J. Colloid Interface Sci. **96**, 251 (1983).

[12] E. J. Meijer and D. Frenkel, Phys. Rev. Lett. **67**, 1110 (1991).

[13] H. N. W. Lekkerkerker, W. C. K. Poon, P. N. Pusey, A. Stroobants, and P. Warren, Europhys. Lett. **20**, 559 (1992).

[14] E. J. Meijer and D. Frenkel, J. Chem. Phys. **100**, 6873 (1994).

[15] M. Dijkstra, J. M. Brader, and R. Evans, J. Phys.: Condens. Matter **11**, 10079 (1999).

[16] P. N. Pusey and W. van Megen, Nature (London) **320**, 340 (1986).

[17] E. R. Weeks, J. C. Crocker, A. C. Levitt, A. Schofield, and D. A. Weitz, Science **287**, 627 (2000).

[18] W. K. Kegel and A. van Blaaderen, Science **287**, 290 (2000).

[19] K. N. Pham, A. M. Puertas, J. Bergenholtz, S. U. Egelhaaf, A. Moussaïd, P. N. Pusey, A. B. Schofield, M. E. Cates, M. Fuchs, and W. C. K. Poon, Science **296**, 104 (2002).

[20] V. J. Anderson and H. N. W. Lekkerkerker, Nature (London) **416**, 811 (2002).

[21] W. Hoover and F. Ree, J. Chem. Phys. **49**, 3609 (1968).

[22] P. J. Lu, E. Zaccarelli, F. Ciulla, A. B. Schofield, F. Sciortino, and D. A. Weitz, Nature (London) **453**, 499 (2008).

[23] E. Sanz, M. Leunissen, A. Fortini, A. van Blaaderen, and M. Dijkstra, J. Phys. Chem. B **112**, 10861 (2008).

[24] S. Tanaka, M. Yamamoto, K. Ito, R. Hayakawa, and M. Ataka, Phys. Rev. E **56**, R67 (1997).

[25] A. Lomakin, N. Asherie, and G. B. Benedek, Proc. Natl. Acad. Sci. U.S.A. **100**, 10254 (2003).

[26] L. F. Filobelo, O. Galkin, and P. G. Vekilov, J. Chem. Phys. **123**, 014904 (2005).

[27] J. F. Lutsko and G. Nicolis, Phys. Rev. Lett. **96**, 046102 (2006).

[28] G. Foffi, C. DeMichele, F. Sciortino, and P. Tartaglia, Phys. Rev. Lett. **94**, 078301 (2005).

[29] P. Charbonneau and D. R. Reichman, Phys. Rev. E **75**, 011507 (2007).

[30] A. Vrij, Pure Appl. Chem. **48**, 471 (1976).

[31] S. Asakura and F. Oosawa, J. Chem. Phys. **22**, 1255 (1954).

[32] F. Sciortino, P. Tartaglia, and E. Zaccarelli, J. Phys. Chem. B **109**, 21942 (2005).

[33] R. Piazza, Curr. Opin. Colloid Interface Sci. **5**, 38 (2000).

[34] N. F. Carnahan and K. E. Starling, J. Chem. Phys. **51**, 635 (1969).

[35] R. Hall, J. Chem. Phys. **57**, 2252 (1972).

[36] D. Frenkel and B. Smit, *Understanding Molecular Simulation 2nd edition*, Vol. 1 of Computational Science Series (Academic Press, New York, 2002).

[37] M. Dijkstra, R. van Roij, and R. Evans, Phys. Rev. E **59**, 5744 (1999).

[38] A. Fortini, A.-P. Hynninen, and M. Dijkstra, J. Chem. Phys. **125**, 094502 (2006).

[39] J. B. Caballero, A. M. Puertas, A. Fernández-Barbero, and F. J. de las Nieves, J. Chem. Phys. **124**, 054909 (2006).

[40] M. P. Allen and D. J. Tildesley, *Computer Simulation of Liquids* (Oxford University Press, New York, 1987).

[41] P. R. tenWolde, M. J. Ruiz-Montero, and D. Frenkel, Phys. Rev. Lett. **75**, 2714 (1995).

[42] U. Gasser, E. R. Weeks, A. Schofield, P. N. Pusey, and D. A. Weitz, Science **292**, 258 (2001).

[43] P. J. Lu, J. C. Conrad, H. M. Wyss, A. B. Schofield, and D. A. Weitz, Phys. Rev. Lett. **96**, 028306 (2006).

[44] P. R. tenWolde and D. Frenkel, Science **277**, 1975 (1997).

[45] A. M. Puertas, M. Fuchs, and M. E. Cates, J. Phys. Chem. B **109**, 6666 (2005).

[46] See EPAPS Document No. E-PLEEE8-78-202809 for movies of the kinetic pathways. For more information on EPAPS, see http://www.aip.org/pubservs/epaps.html.